Published in final edited form as:

IEEE Trans Med Imaging. 2019 September ; 38(9): 2081–2091. doi:10.1109/TMI.2019.2911293.

Quantification of Ventilation and Gas Uptake in Free-Breathing Mice with Hyperpolarized ^{129}Xe MRI

Luis A. Loza,
Department of Radiology, University of Pennsylvania, Philadelphia, PA 19104 USA

Stephen J. Kadlecek,
Department of Radiology, University of Pennsylvania, Philadelphia, PA 19104 USA

Mehrdad Pourfathi,
Department of Electrical and Systems Engineering, University of Pennsylvania, Philadelphia, PA 19104 USA

Hooman Hamedani,
Department of Radiology, University of Pennsylvania, Philadelphia, PA 19104 USA

Ian F. Duncan,
Department of Radiology, University of Pennsylvania, Philadelphia, PA 19104 USA

Kai Ruppert,
Department of Radiology, University of Pennsylvania, Philadelphia, PA 19104 USA

Rahim R. Rizi
Department of Radiology, University of Pennsylvania, Philadelphia, PA 19104 USA

Abstract

Hyperpolarized ^{129}Xe magnetic resonance imaging is a powerful modality capable of assessing lung structure and function. While it has shown promise as a clinical tool for longitudinal assessment of lung function, its utility as an investigative tool for animal models of pulmonary diseases is limited by the necessity of invasive intubation and mechanical ventilation procedures. In this study, we overcame this limitation by developing a gas delivery system and implementing a set of imaging schemes to acquire high-resolution gas- and dissolved-phase images in free-breathing mice. Gradient echo pulse sequences were used to acquire both high- and low-resolution gas-phase images, and regional fractional ventilation was quantified by comparing signal buildup among low-resolution gas-phase images acquired at two flip-angles. Dissolved-phase images were acquired using both ultra-short echo time and chemical shift imaging sequences with discrete sets of flip-angle/repetition time combinations to visualize gas uptake and distribution throughout the body. Spectral features distinct to various anatomical regions were identified in images acquired using the latter sequence, and were used for quantification of gas arrival times for respective compartments.

Luis A. Loza, luisloza@pennmedicine.upenn.edu.

Index Terms-

Xe-129; MRI; lung; hyperpolarized; regional ventilation; free-breathing; gas exchange; image acquisition

I. Introduction

Clinical magnetic resonance imaging (MRI) takes advantage of regional differences in the number of hydrogen atoms and their local magnetic environments to produce anatomical images that differentiate among tissue types. Whereas most organs and tissues are composed of hydrogen-rich water and lipid, the lung consists largely of air, resulting in low signal intensity images of little diagnostic value. Recent advancements in pulse sequence and acquisition procedure techniques, such as ultra-short echo time (UTE) radial k-space acquisitions, arterial spin labelling, and oxygen-enhanced imaging have greatly improved pulmonary imaging in the research domain, providing insight into key structural, ventilation, and perfusion characteristics of the lung, respectively [1]. These approaches are still developing, however, as the long scan times and current spatial coverage are not yet clinically practical [1]. Instead, hyperpolarization (HP) techniques such as spin exchange optical pumping have been developed to enhance the magnetic resonance signal of suitable agents such as ^{3}He or ^{129}Xe gas. When inhaled, these HP species deliver MRI signal gains of approximately 10,000× per nucleus, providing robust images of the lung airspaces in a short time.

HP gas MRI has now been used extensively to probe both structural and functional aspects of the lung. Measuring physiologically relevant parameters such as ventilation [2], oxygenation [3], and lung microstructure [4] enables a more comprehensive assessment of pathological changes than is currently possible with common clinical imaging modalities. HP ^{3}He MRI, for example, has been shown to be more sensitive than spirometry for long-term assessment of functional alterations in the lungs of patients with smoking-related impairment [5], cystic fibrosis [6], and asthma [7]. While animal and clinical studies to date have primarily used ^{3}He [8], the field is gradually shifting to ^{129}Xe in light of both clinical translatability [9] and additional measurements made possible by the gas' dissolution into tissue and blood. Clinical trials have already demonstrated the feasibility of quantifying diffusion and alveolar oxygen tension (PAO_2) using HP ^{129}Xe MRI [10], while assessments based on dissolved ^{129}Xe are sensitive to the primary lung functions of gas exchange and uptake, which could be useful for evaluating lung diseases such as COPD [11] and pulmonary fibrosis [12].

Despite its demonstrated value for the study of lung disease progression, quantitative HP gas MRI studies rely heavily on well-controlled breath volumes and timing. This can be difficult to achieve in human subjects, and is impossible in preclinical animal imaging without mechanical ventilation to precisely control breathing dynamics and enforce breath-holds. Unfortunately, the intubation or tracheotomy required for mechanical ventilation introduces greater variability into these studies: if terminal, larger cohorts are required to account for inter-subject variability; if longitudinal, injury associated with intubation and tracheotomy

[13], or even mechanical ventilation alone, can skew results significantly. Thus, while numerous rodent models of chronic lung diseases such as emphysema [14], [15] and cancer [16] exist, our ability to perform comprehensive longitudinal preclinical research using these models remains severely limited.

In this study, we attempt to overcome the obstacles to longitudinal imaging presented by mechanical ventilation by demonstrating the feasibility of obtaining high-resolution gas-phase (GP) images, fractional ventilation (FV) maps, and time-resolved dissolved-phase (DP) images with HP ^{129}Xe MRI in both healthy wild type mice and genetically modified mice with lung tumors under free-breathing conditions. This work relies on analyses of signal dynamics during ventilation and gas dissolution, and classification based on DP spectral features not previously reported. High-resolution, qualitative GP images were acquired to map ventilation defects, while low-resolution GP images were used to quantify FV. Both UTE and chemical shift imaging (FID-CSI) sequences were used to visualize uptake and transport of dissolved ^{129}Xe. Distinct dissolved state spectral components were visualized separately using an array of repetition time and flip-angle (TR/FA) combinations, highlighting the different arrival and saturation times for each region and blood/tissue type. The comprehensive suite of imaging techniques described here can be applied in the future to the many murine models of lung disease, and can be extended to larger species with modifications to account for tidal volume.

II. Methods

A. Animal Preparation

^{129}Xe imaging was performed on twelve C57BL/6 mice (five each for GP and FID-CSI DP imaging, two for UTE DP imaging). Half of the twelve mice imaged were wild type (C57BL/6^{WT}); the remaining six were a genetically modified C57BL/6 strain (C57BL/6^{mod}) prone to spontaneous tumor induction after orthotopic injection of Cre recombinase via a CMV, SPC, or CC10 vector [17]. All procedures performed were approved by the University of Pennsylvania IACUC (Philadelphia, PA). Animals were anesthetized using 1–2% isoflurane and placed prone in an animal cradle. Positioning on the cradle was adjusted using a bite bar, and an adjustable nose cone slipped over the snout provided gas anesthesia. The animal cradle was then inserted into a double-tuned ^{1}H/^{129}Xe gradient insert before being placed inside the vertical-bore micro-imaging MRI system (Avance 400WB, Bruker Biospin). The RF coil used is approximately 4 cm in length and has an inner diameter of 25 mm: because the RF coil is part of the gradient insert, it is stationary; the bite bar, nose cone, and animal positions can be adjusted to the desired positions. During imaging, the mouse lungs were placed within 1 cm of the center of the coil in order to visualize gas uptake in the lungs and distal regions; both the bite bar and nose cone were outside the RF coil, eliminating the possibility of accidental excitation of HP ^{129}Xe gas during administration and imaging. Temperature and breathing rate were monitored using an endorectal probe and respiratory cushion, respectively.

B. Gas Delivery

85% ^{129}Xe-enriched xenon gas was polarized using a prototype commercial optical pumping system (Xebox E10 Xemed, LLC, Durham, NH) and dispensed into a 0.75 L Tedlar bag within a pressurizable chamber (Fig. 1, green arrows). Typical polarization levels and time required to generate 0.75 L HP ^{129}Xe bags were between 40–50% and 20–25 minutes, respectively. During imaging, flow from this bag was controlled by applying a slight overpressure around the bag. Xenon gas flowed through approximately 1.5m of thin-walled, 1.5875 mm (1/16”) ID PTFA tubing. Steady-state flow was determined by the balance of pressure applied and conductivity of a downstream flow-restricting orifice consisting of approximately 51 mm of 0.254 mm (0.01”) ID, 1.5875 mm (1/16”) OD PEEK tubing (Fig. 1, red arrow). Typical flow rates dispensed the 0.75 L of gas over 25–40 minutes (20–30 cm^3/min), on the same order as the external T1 relaxation of HP ^{129}Xe in the Tedlar bag (approximately 45 minutes).

The tubing passed through a hole down the length of a custom, 3D-printed bite bar (Fig. 1, pink arrows), protruding into the nose cone. The nose cone contained an additional port (Fig. 1, orange arrows) originally designed for delivery of anesthetic gases, but used in this case as an exhaust port through which 120 ml/min of exhaled gas was withdrawn using a peristaltic pump. Because this rate significantly exceeded that of the xenon delivery, the additional gas flow was supplied by flow into the cone past the animal’s head from the airspace in the bore of the magnet (Fig. 1, blue arrows). This region was continuously purged with an air/O_2/isoflurane mixture appropriate for normoxic breathing and stable anesthesia. The setting on the isoflurane vaporizer was adjusted in real time to keep the breathing rate at approximately 120 min^{-1}. Given respective flow rates of 20–30 cm^3/min for HP ^{129}Xe and 120 ml/min for gas withdrawal, the expected partial pressure of ^{129}Xe in the mouse lung is 17–25% during imaging: this value is likely to be slightly higher since the bite bar delivering ^{129}Xe gas points directly at the animal’s mouth.

C. Gas Phase Image Acquisition

Coronal and axial proton T_2-weighted fast spin-echo (FSE) images were acquired for localization. GP and DP images were acquired once steady breathing was attained. GP images were acquired using a respiratory-gated (one phase-encode per breath) slice-selective gradient echo (GRE) pulse sequence (TE = 1 ms, TR = 100 ms, FOV = 20 mm × 20 mm, three 3.4-mm slices, 0 mm slice gap). The pulse shape utilized was calculated using the scanner’s built-in Shinnar-Le Roux algorithm (0.2 ms pulse duration, sharpness = 3, 20 kHz excitation bandwidth, 110.688 MHz center frequency). Although the TR was set to 100 ms, the effective TR between each set of excitations is dependent upon the breathing rate of the animal: e.g., for an average breathing rate of 120 min^{-1}, the TR is approximately 500 ms. High-resolution (matrix size = 96 × 96) GP images were acquired over 4 averages at a fixed flip-angle (FA = 60°); low-resolution (matrix size = 64 × 64) GP images were acquired at two flip-angles (FA = 30°, 90°) for per-breath quantification of FV (see Regional Ventilation Analysis section). Although one set of low-resolution GP images is sufficient to quantify FV, the animal’s variable breathing state throughout image acquisition results in the appearance of motion artifacts. To mitigate such artifacts, 10–15 sets of low-resolution GP images were acquired at each flip-angle in an interleaved manner and later averaged together. At a typical

breathing rate of 120 min^{-1} a high-resolution GP image took approximately 4 × 96 / 120 = 3.2 minutes to acquire, whereas 10–15 sets of low-resolution GP images took no more than 15 × 64 × 2 / 120 = 16 minutes to acquire. Despite the negligible amount of external T1 relaxation of the HP ^{129}Xe during this time, a weighting correction to account for the relaxation was applied to images prior to analysis.

Although dummy scans are necessary to achieve steady state conditions for GP images acquired at FA = 30° (see Regional Ventilation Analysis section), they were not implemented for any acquired GP images. Instead, the GRE sequence used first sampled points at high values of k-space, providing enough time for alveolar magnetization to reach steady state and producing a minimal contribution to overall image signal.

D. Dissolved Phase Image Acquisition

GP and DP images were acquired using two methods. The first method involved separate acquisitions using either a UTE or FID-CSI sequence. Selective excitation was implemented using a customized UTE pulse sequence to simultaneously acquire GP and DP images (TE = 0.1 ms, TR = 50 ms, 100 ms, FA = 20°, 40°, 70°, FOV = 35 mm × 25 mm, matrix size = 128 × 128, 402 radial spokes, projection). The pulse shape utilized was calculated by the scanner's Shinnar-Le Roux algorithm as previously mentioned (0.15 ms pulse duration, sharpness = 1, 14 kHz excitation bandwidth, 110.709 MHz center frequency).

GP and DP images were also acquired using an FID-CSI sequence with a custom-phase encode table (TE = 0.5 ms, TR = 80 ms, FA = 10°, 20°, 40°, 70°, 90°, FOV = 35 mm × 20 mm, matrix size = 64×36, projection, Gaussian pulse shape, 0.1 ms pulse duration, 27 kHz excitation bandwidth, 110.709 MHz center frequency). The pulse sequence applied was developed such that we excited the GP resonance at approximately 7.7% of the nominal flip-angle excitation applied to DP resonances. This was implemented in order to avoid depletion of HP ^{129}Xe magnetization before it entered the DP. The narrow range of DP resonances ensured that there was negligible variation in the excitation profile among the dissolved peaks. Dummy scans were not included in either of these sequences; however, UTE images were acquired over eight averages, while FID-CSI images utilized oversampling of k-space points near 0 in a randomized order to mitigate signal artifacts. ^{129}Xe uptake and transport throughout the body were followed by altering TR/FA combinations to control the rate of RF-induced ^{129}Xe relaxation (see Dissolved Phase Signal Analysis section).

The second method involved implementing a continuous, variable flip-angle scan to acquire GP and DP images. GP and DP image sets were acquired by implementing a FID-CSI sequence using a custom phase-encode/flip-angle table (FA = 6°, 12°, 25°, 50°, 90°, the remaining parameters used were the same as those implemented in the previously described CSI). Each image utilized a total of 2688 k-space points, and potential motion artifacts were mitigated by oversampling points near the center of k-space in a randomized order. The k = 0 point was sampled 64 times whenever the flip-angle was changed to account for the external magnetization decay of the HP ^{129}Xe gas and to ensure that steady-state ^{129}Xe magnetization conditions were achieved throughout the body (Fig. 2). These acquisitions were not used in image reconstruction. Lower flip-angle acquisitions were repeated (three times for FA = 6°, twice for FA = 12°) to ensure adequate signal-to-noise. Since the animal's

respiratory state can vary during imaging, we did not acquire complete images before changing the flip-angle; instead, each image was divided into eight groups of k-space points (336 points per group) and acquired in an interleaved manner, ensuring that different breathing states were equally represented in each image.

1H B0 maps were also separately acquired to determine the homogeneity of our field and its effect on dissolved HXe resonance peak assignments (see Dissolved Phase Signal Analysis section). Since quantitative analysis was only applied for FID-CSI-acquired images, B0 maps were acquired for a FOV of 35 mm × 20 mm; the largest frequency shift observed in this region was no more than 201 Hz (approximately 0.5 ppm). Additionally, a flip angle calibration was performed on a HP ^{129}Xe gas phantom; measured flip angles within 30 mm of the center of the coil were within 10% of the nominal value, which could lead to errors of up to 20% in the nominal RF-induced relaxation rate (see Dissolved Phase Signal Analysis section).

E. Signal Buildup Analysis and Modeling

1) Regional Ventilation Analysis—Specific ventilation (SV) is defined as the ratio of fresh, per-breath gas reaching a region of interest to the gas present at end-exhale, while FV is the ratio of that same fresh gas to the gas present at end-inhale, with the relation between the two being $SV = \frac{FV}{1-FV}, FV = \frac{SV}{1-SV}$. SV is the most widely accepted measurement of regional ventilation, and thus its derivation is shown here; however, the range of values derived from SV measurements are on a zero to infinity scale, creating difficulties in both presentation and interpretation. Conversely, FV measurements are on a 0 to 1 scale, and are presented in the Results section for ease of presentation and interpretation.

Because acquisitions are performed in steady-state, the gas signal observed during each acquisition reflects a balance between magnetization gained through the inhalation of fresh HP ^{129}Xe from the gas stream and magnetization lost through a combination of exhalation, RF-induced relaxation, relaxation due to collisions with paramagnetic O_2 molecules and alveolar walls, and magnetization that enters the DP. A previously published analytical model of gas replacement and relaxation [18] showed that after n identical breaths imaged with flip-angle α at a specific ventilation SV from a source magnetization M_S, local alveolar magnetization M_A will be:

$$M_A(n) = \frac{SV}{1 + SV - \cos(\alpha)f}\left(1 - \left(\frac{\cos(\alpha)f}{1+SV}\right)^n\right)M_S \quad (1)$$

in which f refers to the remaining magnetization after one breath in the absence of gas replacement by breathing or RF pulse application [18]. Previous schemes to isolate SV have imaged during breath-hold and either eliminated or accounted for the effect of RF pulses [19], [20]. However, such approaches are difficult to implement for a free-breathing mouse. Instead, we spread the image over multiple steady-state breaths, acquiring one line of k-space per breath. In this case, the magnetization of each image is approximated by the limit of (1) for large n:

$$M_{A,\,steady\,state} = \frac{SV}{1 + SV - \cos(\alpha) f} M_S \tag{2}$$

and the corresponding signal intensity S varies with α as:

$$S(\alpha) = \frac{(1 + SV)\sin(\alpha)}{1 + SV - \cos(\alpha) f} S_{90} \tag{3}$$

where S_{90} refers to the signal intensity that would be observed if a 90-degree pulse were applied after each breath. For the rapidly-breathing mouse and practical excitation schemes, RF pulse-induced magnetization loss substantially exceeds that due to other processes. We can therefore estimate local SV by comparing images at different flip-angles.

Fig. 3A summarizes steady-state signal's dependence on applied flip-angle for a wide range of SV values. Note that, in practice, maximum signal is seen when per-breath gas replacement is approximately equal to the RF-induced relaxation cos(α). Although it is possible to map the entire flip-angle dependence by acquiring images with a variety of α, this is not necessary to determine SV: the ratio between two image intensities is sufficient and, among the schemes we have explored, optimal for this purpose. For simplicity, we have fixed one of these excitations at 90° and refer to the other chosen flip-angle as α_{ref}. SV may be calculated by inverting (3) in terms of the ratio of the image intensities $R = S(\alpha_{ref}) / S(90)$:

$$SV = \frac{\sin(\alpha_{ref}) - R(1 - f\cos(\alpha_{ref}))}{R - \sin(\alpha_{ref})} \tag{4}$$

The most noise-insensitive choice of α_{ref} depends on the expected SV range; simulations of this dependence indicate that a low α_{ref} is best suited to accurate measurements of low SV, with the optimal choice for α_{ref} increasing from approximately 8° at SV = 0.01 to 25° at SV = 0.1 (Fig 3A). Previous studies have reported FV values of 0.21 ± 0.09 and 0.34 ± 0.01 in mice, respectively, yielding a plausible FV range of 0.12 – 0.35, or 0.14 – 0.54 in SV [21], [22]. We have chosen α_{ref} = 30° to maintain acceptable accuracy throughout this physiologically-expected range (Fig. 3B). We assume f to be dominated by O_2-induced relaxation and can therefore estimate its value based on the expected ~13.3 kPa PAO_2 in the lung and previous measurements of spin relaxation during ^{129}Xe-O_2 collisions [23]; $f \cong \exp\left(-\frac{60}{BPM} \times \frac{13.3\,kPa}{101.3\,kPa} bar \times \frac{0.3934}{s\,atm}\right) = 0.975$ at the targeted 120 breaths per minute. As it is quite close to 1, we find that in practice including the correction factor f to be only marginally significant, and only for SV < 1. Fig. 3B summarizes the expected error in SV due to misestimation of f and instrumental noise, appropriately drawn from a Rician distribution [24] when using (4).

2) Dissolved Phase Signal Analysis—Unlike ^{3}He, ^{129}Xe gas dissolves into tissue and blood when inhaled. Approximately 1–2% of inhaled ^{129}Xe dissolves into blood [25] and is carried from the lungs to the heart and throughout the rest of the body. GP ^{129}Xe resonates at a single frequency, nominally set at 0 ppm, whereas DP ^{129}Xe presents multiple

peaks offset from the gas frequency by 185 – 221 ppm, associated with distinct tissue types and anatomical regions. The presence and location of these DP peaks is species dependent; mice present peaks ranging from 185 – 205 ppm, whereas rats and humans present peaks ranging from 192 – 221 pm [26], [27].

The uptake and transport of dissolved HP ^{129}Xe to regions at different distances from the lungs can be visualized by acquiring images using different TR/FA combinations [28]. By analogy with the SV imaging above, TR/FA combinations that induce less decay allow HP ^{129}Xe magnetization to persist long enough to travel further along the circulatory system and into more distal tissue. Conversely, TR/FA combinations that induce more decay "use up" dissolved ^{129}Xe magnetization at a quicker rate, emphasizing the lung parenchyma and immediately accessible structures.

All DP images were acquired during a continuous administration of HP ^{129}Xe during which a steady-state concentration of the dissolved gas is likely achieved throughout the animal's body. Nonetheless, flow or exchange into and out of each anatomical structure proceeds at a different rate and with different timing with respect to the moment of dissolution. In general, dissolved ^{129}Xe signal from a particular location will arise from atoms that have been dissolved for various lengths of time t, distributed as an unknown function that we refer to as $T(t)$. Measuring this time distribution has the potential to highlight gas uptake, diffusion, or blood flow characteristics that may be indicative of pathology.

We may impose sensitivity to $T(t)$ by comparing images acquired with different RF-induced relaxation rates $T_{1,RF}$, which we approximate as $T_{1,RF} = \mathrm{TR}/[1-\cos(\alpha)]$ as per [29]. The observed signal intensity will then depend on applied RF as

$$\frac{S(T_{1,RF})}{\sin(\alpha)} \sim \int_0^\infty T(t)\exp(-t/T_1)\exp(-t/T_{1,RF}) \tag{5}$$

This expression is formally a Laplace transform; given sufficient measurements of $S(T_{1,RF})$, and knowledge or assumptions about T_1, the signal relaxation rate in the absence of applied RF (5) can be inverted to completely specify $T(t)$. In practice, limitations to the number of images that can be feasibly acquired, coupled with the wide range of signal buildup times that may be of interest, make this process difficult. We thus parameterize $T(t)$ in terms of its first two moments to extract the value of most interest, $\bar{T}$, or the mean time between dissolution and arrival at the anatomical compartment of interest

$$T(t) = \frac{1}{\sqrt{\pi\sigma^2}}\exp\left[-\left(t-\bar{T}\right)^2/\sigma^2\right] \tag{6}$$

and fit to the measured $S(T_{1,RF})$, allowing $\bar{T}$ and the breadth of the distribution σ^2 to vary. Interpreting $\bar{T}$ depends on the dissolved gas dynamics of the structure being investigated: in vascular compartments, it is likely most closely associated with the time required for saturated blood to reach the structure after leaving the lungs; in tissue and lipid compartments, it is likely more representative of gas exchange time.

The above analysis was attempted using both FID-CSI and UTE images, the latter of which were more difficult to compare quantitatively given fluctuations in the animal's breathing pattern as well as disparities in signal intensity among images due to T_1 decay during imaging. DP image sets acquired using our FID-CSI method were much more comparable, as the interleaved pattern ensured that each image sampled approximately equally from all of the variable animal and HP agent states.

After acquisition, CSI images' FID signal levels were normalized to account for polarization decay. Excluding those acquired while approaching steady-state, FIDs corresponding to a given flip-angle/phase-encoding pair were averaged, assembled into a 3D array, and Fourier transformed to yield individual maps of ^{129}Xe magnetization. After line broadening by 50 Hz (~0.5 ppm), individual maps were generated by integrating spectral lines corresponding to the GP resonance (with the gas resonance center at 0 ppm by definition) and the DP resonances (185 to 205 ppm). All complex ^{129}Xe spectra were well described by four individual Lorentzian resonance lineshapes and center frequencies, corresponding to dissolved gas in different compartments. As previously described [30], [31], three of these compartments corresponded to ^{129}Xe dissolved in vascular blood, high-lipid-content "fat," and low-lipid-content solid organ "tissue," respectively. A fourth component, at the same center frequency as vascular blood but with a much broader linewidth, corresponded to parenchymal lung tissue in which magnetic field heterogeneity is high due to air/tissue interfaces. Line amplitudes, center frequencies, linewidths, and phases were individually extracted using a least-squares fit to the real and imaginary components of each spectra, producing individual maps for the four components as a function $T_{1,RF}$.

F. Image Registration

Image analysis and registration was performed using custom software developed using MATLAB (MathWorks, Inc., Natick, MA). GP images acquired using the same flip-angle were averaged and bias-corrected based on the background noise. An atlas of the lung was generated by summing individual GP images and applying a smoothing Gaussian filter, to which all lungs were registered. Registered images were normalized to their respective maximum signals and added together; a contrast limited adaptive histogram equalization (CLAHE) with a gray-scale threshold was then applied to mask the background noise and segment the lung [32].

III. Results

T_2-weighted proton images, high-resolution GP images, and low-resolution GP images to derive FV were acquired in two C57BL/6^{WT} control mice and three C57BL/6^{mod} mice with lung tumors. Fig. 4 depicts three representative mice: one control animal (Row A) and two of those with tumors (Rows B and C). As expected, the GP image in row A shows a homogenous distribution of gas with no ventilation defects. GP images in rows B and C, however, exhibit heterogeneous gas distribution. Areas of completely compromised ventilation correlate well with regions of cancer (white arrows), although the smaller tumors present in the animal in row C lead to a less pronounced signal loss due to partial volume effects in the HP gas slice.

FV maps and corresponding histograms are also shown in Fig. 4. The FV map in row A shows a narrow and symmetric distribution of values, and the mean FV (0.35 ± 0.07) correlates well with the overall shape of the histogram. The FV map in row B, however, displays a heterogeneous distribution of values, especially near regions of cancer; this heterogeneity is reflected in the histogram, which exhibits one prominent peak at FV = 0.4, with a smaller secondary peak at FV = 0.3 attributable to decreased FV in tumor-adjacent regions. The heterogeneity in FV is not immediately evident when looking at the mean FV (0.37 ± 0.08, 0.34 ± 0.13 when including regions of completely compromised ventilation). The FV map in row C also shows a heterogeneous distribution of values, with several apparent voids corresponding to tumor regions. While histogram C is similar in shape to histogram A, it is centered at a slightly higher value (mean FV of 0.44 ± 0.07, 0.41 ± 0.13 when including regions of completely compromised ventilation). The heterogeneity in FV is most apparent when looking at the "tail" of lower FV values in the histogram, qualitatively similar to that of row B but with a reduced effect on ventilation as befitting the smaller tumor size.

DP images were acquired in seven mice (one C57BL/6^{WT} and one C57BL/6^{mod} mouse for UTE imaging, three C57BL/6^{WT} and two C57BL/6^{mod} mice for CSI imaging) at various TR/FA combinations. Fig. 5 depicts representative images acquired in two C57BL/6^{mod} mice using both sequences. The representative datasets are ordered by increasing $T_{1,RF}$; as previously described [28], this one parameter summarizes the effect of changing either TR or FA, allowing both qualitative and quantitative comparisons of images acquired using different parameters.

Both image sets display qualitatively similar behavior: as $T_{1,RF}$ increases, structures become visible in the order that gas taken up by the lung reaches them. Parenchymal tissue (left) is saturated first, followed by the lung vasculature and left atrium (~150 ms), left ventricle (~200 – 300 ms), aortic arch (400 – 500 ms), and descending aorta (700 – 800 ms). When $T_{1,RF}$ is increased beyond a few seconds, the kidneys, diffuse tissue structures, and vena cava become apparent as well.

Analysis of DP CSI images revealed three dominant spectral features, one of which was further separated into two distinct contributions based on linewidth in the lung parenchyma. Fig. 6 shows this linewidth distinction and its use for differentiating the heart and vasculature from the spatially intertwined but physiologically distinct lung parenchyma in an image acquired in a C57BL/6^{WT} mouse with a moderate $T_{1,RF}$ of 1.3s. A narrow contribution (< 100 Hz, Fig. 6A) was seen only in regions that corresponded anatomically to the heart or vasculature, whereas a broad component (> 250 Hz, Fig. 6B) arose from the short-T_2*, magnetically inhomogeneous parenchymal tissue of the lung. Voxels containing both features were characterized by a superposition of the two lineshapes rather than by a single line of intermediate width, thereby allowing for a clear, separate visualization of the lung parenchyma and heart/vasculature.

As $T_{1,RF}$ increases and additional structures fill with ^{129}Xe magnetization, spectral analysis becomes more complicated. Fig. 7 shows the real components of NMR spectra acquired in a C57BL/6^{mod} mouse from ten anatomical regions of interest: lung parenchyma (top left), left

ventricle, aortic arch, abdominal aorta (top, columns 2–4), a region of fat tissue (top right), liver (bottom left), kidneys (bottom, columns 2–3), heart wall (bottom, column 4) and vena cava (bottom right). The five spectra from each region, acquired bottom to top with increasing $T_{1,RF}$, show an increase in both ^{129}Xe magnetization present and spectral complexity as magnetization accumulates throughout the body.

Unsurprisingly, magnetization is present in the lung parenchyma immediately after dissolution (top left, $T_{1,RF}$ = 80 ms), appearing in a broad line at the central frequency of 194.5 ppm. Signal appears next at the same frequency in the pulmonary veins, left atrium and left ventricle, followed closely by other vascular components. Additional resonances are evident much later at the kidneys, heart wall, and liver (~5 ppm higher) as well as in lipid (~3.4 ppm lower), suggesting the possibility of separately determining the dynamic characteristics of each of the four spectral components for each voxel or region of interest, even if the contributions are spatially co-localized. For instance, spectra acquired in organ tissue depict the arrival of ^{129}Xe in the blood after a few hundred milliseconds (e.g., purple and yellow spectra in the bottom row of Fig. 7), followed by exchange of that signal into the tissue spectral compartment over several seconds, as seen in the growth of the leftmost peak. Of particular interest is the clearly discernable change in chemical shift between arterial and venous blood (Fig. 7, top row vs. bottom right). Blood in the vena cava and right heart appears at a frequency 1.0 ppm higher on average than that in the descending/abdominal aorta and the left heart.

Fig. 8 shows the production of individual spectrally-resolved maps for a dataset acquired in the same animal as in Fig. 7. Images acquired with $T_{1,RF}$ values ranging from 80 ms (top row) to 14.6 s (bottom row) depict reconstructions of the GP spectral region (left column), the total integrated DP spectral region (column 2), and DP spectral components generally characterized as lung parenchyma, heart/vasculature, lipid, and organ/muscle tissue (columns 3–6). The large range of distinct chemical shifts among various anatomical regions allows separate visualization of each spectral component contribution, as illustrated by respectively colored DP images. Note that each spectral component has both a distinct spatial distribution and unique dependence on $T_{1,RF}$, indicating distinct dissolved gas arrival times and tissue saturation characteristics. Signal is at near-maximum intensity in lung parenchymal tissue as soon as 80 ms after inhalation of ^{129}Xe gas, whereas it is not seen in the parenchymal vasculature and heart for approximately 200 ms. Regions further from the lung, such as lipid and distal organs/tissue, require longer signal buildup times before visualization is possible. The heart wall, which shares the spectral characteristics of other perfused tissue (rightmost row), is not clearly visible until several seconds have elapsed despite the fact that signal can be seen to arrive in the heart chamber after only a fraction of a second. As with the kidneys, liver, and other tissues, this muscular structure is not conspicuous in any of the total DP images; separation based on spectral characteristics is therefore necessary to observe this distinctive behavior.

Frequency also distinguishes additional sub-compartments within the broad spectral characterization outlined above. The heart and vasculature resonance is clearly delineated between oxygenated blood (194.5 ppm, Fig. 8, red) primarily localized in the left heart, aortic arch, descending/abdominal aorta and carotid artery, and deoxygenated blood (195.5

ppm, blue) in the right heart, vena cava, and jugular vein. The organ and tissue compartment is also subject to a slight frequency variation distinguishing heart wall and kidneys (199.6 ppm, ochre) from liver and chest wall musculature (200.8 ppm, purple).

Once distinguished visually, it is possible to quantify the temporal behavior of each anatomical compartment in the manner shown in Fig. 9. Here, one peak is selected for each of the ten structures displayed in Fig. 7: the narrow blood peak of the oxygenated heart/vascular compartments (left ventricle, aortic arch, and descending/abdominal aorta) is displayed in red, the tissue peak in the heart wall and kidneys is shown in ochre, and the lipid peak in fat regions in cyan. Integrals of the respective peaks for a single dataset are fit to the model of (5) and (6) from which mean dissolved gas arrival time is extracted.

IV. Discussion

In this study, we demonstrated the feasibility of quantifying FV and gas arrival times in free-breathing mice using high-resolution GP and DP images acquired via HP ^{129}Xe MRI using a custom-built continuous gas delivery system combined with variable flip-angle pulse sequences. Despite the successful study of animal models of lung disease using HP gas MRI for over twenty years, the necessary use of anesthesia, terminal tracheotomy or intubation, and mechanical ventilation to control gas administration has severely limited its use for the kind of longitudinal imaging studies needed to better interrogate disease models characterized by high inter-subject variability-such as lung cancer or COPD-in which understanding disease progression is essential for planning treatment and monitoring functional response. Airway and lung damage caused by intubation and mechanical ventilation in small animals is often significant enough to preclude longitudinal studies [13], whereas altered breathing mechanics combined with the risk of ventilator-induced lung injury make them difficult to perform and interpret even in larger animal species. Given the wide variety of available pathological disease models which use genetically engineered mice, a non-terminal, minimally invasive imaging protocol that enables longitudinal studies will be of particular value to researchers.

Several HP ^{129}Xe MRI and MRS studies using free-breathing murine models precede this work. A group at Osaka University developed a continuous-flow hyperpolarization system [33], [34] that has been applied to measurements of HP ^{129}Xe signal dynamics [35], [36], GP and DP imaging [33], measurements of regional pulmonary ventilation [21], [37], [38], and assessments of lung function in mouse models of emphysema [21], [38], [39] and lung cancer [16]. Various methods for measuring FV using ^{3}He MRI have also been published. Deninger et al. were the first to report measurement of regional pulmonary ventilation in guinea pigs using a mathematical model to describe magnetization buildup after a discrete number of ^{3}He breaths [20]. Emami et al. then presented a more gas-efficient imaging scheme, applicable in large animals and humans, to acquire images after a single series of ^{3}He gas breaths [19]. While both methods produce robust FV maps, their gas delivery and imaging protocols rely heavily on mechanical ventilation to control gas administration as well as to synchronize breath and MRI acquisition.

To our knowledge, Imai and Hori et al. were the first to demonstrate measurements sensitive to ventilation in free-breathing mice using ^{129}Xe MRI. The first method described [37] is most similar to that presented here, using analysis of three images acquired with different flip-angles to yield a regional signal recovery time due to ventilation. Subsequent studies used end-inspiration and end-expiration GP images to calculate regional ventilation [38], as well as a fit of GP images acquired after various numbers of xenon breaths to signal buildup curves [21], [37] in the manner described by Deninger and Emami. Although these techniques enabled measurements of regional pulmonary ventilation, our method is distinguished by its relative simplicity, requiring only a ratio of two images, a quantitative connection to FV or SV, and spatial resolution consistent with imaging of small defects. Improved resolution (0.3 mm^2 vs. 0.8mm^2 [21] and 1.0mm^2 [38] in Imai, et al., 0.7mm^2 in Deninger [20] and 0.9mm^2 in Emami [19]) is achieved in part via consistent use of isotopically enriched gas, overall higher polarization levels than were previously obtainable, and in some cases longer signal-averaging periods. Given the potential for anesthetic and other physiological variability, these longer acquisition periods also allowed selection of image sets that were well matched with respect to breathing rate.

Quantitative comparison of FV in mechanically ventilated animals is difficult due to significantly larger airway sizes and lung volumes [40]. Such studies also tend to image at an end-inhale breath-hold, leading to different values in airways that are completely filled with fresh gas, rather than exhaled residual gas present at the quiescent end-expiratory period. Given FV measurements' sensitivity to ventilation parameters such as tidal volume [19], discrepancies in FV for free-breathing vs. mechanically ventilated animals are expected; indeed, FV variability is seen even between studies employing similar mechanical ventilation protocols. For example, Santyr [41] and Couch [42] reported FV values using ^{3}He in rats that were in agreement with a nominal value of 0.4 ± 0.1 [43], whereas Stephen reported a mean FV of 0.58 ± 0.03 [44].

This uncertainty in mean FV does not negate the utility of these measurements, however, as heterogeneity of FV maps and mean values among subjects within the same study still provides researchers with valuable information. For example, several studies showed the utility of FV measurements in detecting and assessing impaired lung function between healthy and sick mice in models of asthma [22] and emphysema [15]. Similarly, while our mean FV values were not significantly different between healthy and sick mice, the heterogeneity within FV maps-specifically the lack of ventilation in regions of lung cancer (Fig. 4B and 4C)-is indicative of impaired lung function. This is primarily reflected in reduced ventilation in regions near the tumor (e.g., Fig. 4A vs. 4B) and associated skewing of the FV distribution toward lower values.

In addition to the GP imaging used to generate FV maps, DP imaging was also performed on mice using both UTE and CSI sequences with a constant TR and varying flip-angles. As Fig. 5 shows, lower flip-angle images display features farther away from the lungs (i.e. heart structures, lipid, abdominal regions), whereas high flip-angle images highlight features closer to the lung parenchyma. Although both sequences are capable of acquiring GP and DP images simultaneously, we found that the CSI sequence was superior for visualizing

xenon gas uptake and distribution due to the additional spectral information it provides, which is crucial for separating the lungs, heart, and distal regions from one another.

The unique spectral lineshape that dissolved HP ^{129}Xe presents for particular anatomical regions enables separate visualization of different tissue types and quantification of gas arrival/exchange dynamics. Matching distinct lineshapes to their respective functional compartment is relatively simple for regions near the lungs; however, as xenon dissolves into additional anatomical compartments and the number of spectral contributions at similar chemical shifts increases, distinguishing these contributions from one another using total DP signal becomes nearly impossible, especially for overlapping anatomical compartments (Fig. 7). To overcome this difficulty, we identified distinct, regional spectral contributions based on line amplitude, lineshape, center frequency, and phase. Observed spectral contributions for high flip-angle images (where dissolved ^{129}Xe only reaches the lungs) are clearly from the lungs; moving to lower flip-angles where additional spectral contributions become present, we can build on knowledge of identified lineshapes to decouple additional, spatially overlapping spectral contributions. Distinguishing between these spectral features is likely necessary to meaningfully quantify signal dynamics, as each component may display different temporal behavior. Although not yet studied in detail, one possible use of the timing information shown here is to further understand the rate and heterogeneity of pulmonary gas uptake and delivery to perfused tissues, and its dependence on physiological or disease state.

Both previous ^{129}Xe spectral measurements in rodents and non-imaging investigations of blood desaturation during an extended breath-hold have demonstrated the broad discrimination into blood, lipid, and tissue compartments shown here [31], [45]. To our knowledge, however, quantitative imaging of ^{129}Xe resonance frequency changes with blood oxygenation and tissue type has not been reported before. Some animals, including humans, display separate resonances associated with red blood cells (hemoglobin binding) and blood plasma/lung parenchymal tissue [11], [25], [45]. This distinction is not present in mice, and we observed no systematic difference between the resonance frequency of vascular blood anywhere in the body and the broad resonance corresponding to lung parenchymal tissue. In vitro measurements of frequency shifts associated with human blood oxygenation have also been reported [27] and it is worth noting that the shift clearly observed in this study is in the opposite direction from that seen in human blood, highlighting this interaction’s sensitivity to subtle changes in hemoglobin structure and its conformational changes in response to oxygen binding. Other aspects of the interaction in distinct species, including binding affinity, bound-free exchange rate, and signal loss rates in oxygenated/deoxygenated blood will require separate study in future in vitro experiments.

Although imaging during free-breathing provides the most accurate representation of the lung in its natural state, this technique also suffers from several limitations. While the use of isoflurane keeps animal breathing patterns relatively steady, sporadic variations in breathing rate and depth during imaging are inevitable and can lead to motion artifacts and blurring, despite k-space order randomization and oversampling. Image registration prior to analysis mitigates major motion artifacts, but imperfect registration can also introduce errors. The mouse’s breathing rate must also be kept within a reasonable range: when too fast, FV image

acquisition occurs over multiple breaths as opposed to per-breath, as modeled; when too slow, FV acquisition time is dramatically extended and DP images suffer from poor signal-to-noise.

It is also important to note limitations associated with interpreting the signal buildup times of Fig. 9. Although measurements were quite consistent among experimental animals, a large number of $T_{1,RF}$ values would be needed to accurately constrain the large range of buildup times of interest. In our study, the largest value utilized was of the same order as the observed signal buildup in fat tissue. Thus, signal saturation was never fully achieved, adding uncertainty to the fit and subsequent extraction of the signal buildup time constant. Further, the apparent signal saturation time is expected to be smaller than the true xenon concentration buildup time due to relaxation of the HP state in the target tissue of interest. The relaxation rate (T_1) likely depends on tissue type, but is not generally known for all of the structures investigated here. Although published measurements vary greatly (e.g., [46], [47]), all T_1 values likely exceed the apparent buildup time constraints in tissues of interest ([46], [48]), but not sufficiently to avoid bias. Where signal arrival is significantly faster than either (e.g., heart or vascular structures), signal saturation is complete for the larger $T_{1,RF}$ values and neither source of uncertainty is significant.

Acknowledgments

The transgenic mouse model used was kindly provided by Dr. Diane Lim from the Department of Sleep Medicine at the University of Pennsylvania located in Philadelphia, PA, 19104 United States.

This work was supported in part by the U.S. National Institute of Health under Grant R01 CA193050, Grant S10 OD016332, and Grant S10 OD018203.

VI. References

[1]. Miller GW, Mugler JP, Sá RC, A Altes T, Prisk GK, Hopkins SR, “Advances in functional and structural imaging of the human lung using proton MRI,” NMR in Biomedicine, vol. 27, no. 12, pp. 1542–1556, 12 2014. [PubMed: 24990096]

[2]. Hamedani H, Clapp JT, Kadlecek SJ, Emami K, Ishii M, Gefter WB, Xin Y, Cereda M, Shaghaghi H, Siddiqui S, et al., “Regional fractional ventilation by using multibreath wash-in ^{3}He MR imaging,” Radiology, vol. 279, no. 3, pp. 917–924, 6 2016. [PubMed: 26785042]

[3]. Hamedani H, Kadlecek SJ, Ishii M, Xin Y, Emami K, Han B, Shaghaghi H, Gopstein D, Cereda M, Gefter WB, et al., “Alterations of regional alveolar oxygen tension in asymptomatic current smokers: Assessment with hyperpolarized He-3 MR Imaging,” Radiology, vol. 274, no. 2, pp. 585–596, 2014. [PubMed: 25322340]

[4]. Hamedani H, Kadlecek S, Xin Y, Siddiqui S, Gatens H, Naji J, Ishii M, Cereda M, Rossman M, Rizi R, “A hybrid multibreath wash-in wash-out lung function quantification scheme in human subjects using hyperpolarized ^{3}He MRI for simultaneous assessment of specific ventilation, alveolar oxygen tension, oxygen uptake, and air trapping” Magnetic Resonance in Medicine, vol. 78, no. 2, pp. 611–624, 8 2017. [PubMed: 27734519]

[5]. Fain SB, Panth SR, Evans MD, Wentland AL, Holmes JH, Korosec FR, O’Brien MJ, Fountaine H, Grist TM, “Early emphysematous changes in asymptomatic smokers: Detection with ^{3}He MR Imaging,” Radiology, vol. 239, no. 3, pp. 875–883, 6 2006. [PubMed: 16714465]

[6]. Smith L, Marshall H, Aldag I, Horn F, Collier G, Hughes D, West N, Horsley A, Taylor CJ, Wild J, “Longitudinal assessment of children with mild cystic fibrosis using hyperpolarized gas lung Magnetic Resonance Imaging and Lung Clearance Index,” American Journal of Respiratory and Critical Care Medicine, vol. 197, no. 3, pp. 397–400, 2 2018. [PubMed: 28661699]

[7]. Fain SB, Gonzalez-Fernandez G, Peterson ET, Evans MD, Sorkness RL, Jarjour NN, Busse WW, Kuhlman JE, “Evaluation of structure-function relationships in asthma using multidetector CT and hyperpolarized He-3 MRI,” Academic Radiology, vol. 15, no. 6, pp. 753–762, 6 2008. [PubMed: 18486011]

[8]. Roos JE, McAdams HP, Kaushik SS, Driehuys B, “Hyperpolarized gas MR Imaging,” Magnetic Resonance Imaging Clinics of North America, vol. 23, no. 2, pp. 217–229, 5 2015. [PubMed: 25952516]

[9]. Driehuys B, Martinez-Jimenez S, Cleveland ZI, Metz GM, Beaver DM, Nouls JC, Kaushik SS, Firszt R, Willis C, Kelly KT, et al., “Chronic obstructive pulmonary disease: Safety and tolerability of hyperpolarized ^{129}Xe MR Imaging in healthy volunteers and patients,” Radiology, vol. 262, no. 1, pp. 279–289, 1 2012. [PubMed: 22056683]

[10]. Ouriadov A, Farag A, Kirby M, McCormack DG, Parraga G, Santyr GE, “Pulmonary hyperpolarized Xe-129 morphometry for mapping xenon gas concentrations and alveolar oxygen partial pressure: Proof-of-concept demonstration in healthy and COPD subjects” Magnetic Resonance in Medicine, vol. 74, no. 6, pp. 1726–1732, 12 2015. [PubMed: 25483611]

[11]. Mugler JP, Altes TA, Ruset IC, Dregely IM, Mata JF, Miller GW, Ketel S, Ketel J, Hersman FW, Ruppert K, “Simultaneous magnetic resonance imaging of ventilation distribution and gas uptake in the human lung using hyperpolarized xenon-129,” Proceedings of the National Academy of Sciences, vol. 107, no. 50, pp. 21707–21712, 12 2010.

[12]. Lilburn DML, Pavlovskaya GE, Meersmann T, “Perspectives of hyperpolarized noble gas MRI beyond 3He,” Journal of Magnetic Resonance, vol. 229, pp. 173–186, 4 2013. [PubMed: 23290627]

[13]. Fox MS, Welch I, Hobson D, Santyr GE, “A novel intubation technique for minimally invasive longitudinal studies of rat lungs using hyperpolarized ^{3}He magnetic resonance imaging,” Laboratory Animals, vol. 46, no. 4, pp. 311–317, 10 2012. [PubMed: 23097565]

[14]. Ford NL, Martin EL, Lewis JF, Veldhuizen RAW, Holdsworth DW, Drangova M, “Quantifying lung morphology with respiratory-gated micro-CT in a murine model of emphysema,” Physics in Medicine and Biology, vol. 54, no. 7, pp. 2121–2130, 4 2009. [PubMed: 19287083]

[15]. Imai H, Kimura A, Iguchi S, Hori Y, Masuda S, Fujiwara H, “Noninvasive detection of pulmonary tissue destruction in a mouse model of emphysema using hyperpolarized 129Xe MRS under spontaneous respiration,” Magnetic Resonance in Medicine, vol. 64, no. 4, pp. 929–938, 8 2010. [PubMed: 20740664]

[16]. Imai H, Kimura A, Ito T, Fujiwara H, “Hyperpolarized 129Xe dynamic study in mouse lung under spontaneous respiration: Application to murine tumor B16BL6 melanoma,” European Journal of Radiology, vol. 73, no. 1, pp. 196–205, 1 2010. [PubMed: 19010631]

[17]. Sheen MR, Marotti JD, Allegrezza MJ, Rutkowski M, Conejo-Garcia JR, Fiering S, “Constitutively activated PI3K accelerates tumor initiation and modifies histopathology of breast cancer,” Oncogenesis, vol. 5, no. 10, pp. e267–e267, 10 2016. [PubMed: 27797363]

[18]. Kadlecek S, Rizi RR, Albert MS, Hane FT. “Quantitative ventilation imaging using hyperpolarized gas and multibreath imaging sequences,” in Hyperpolarized and inert gas MRI: From technology to application in research and medicine, Academic Press, 2016.

[19]. Emami K, Kadlecek SJ, Woodburn JM, Zhu J, Yu J, Vahdat V, Pickup S, Ishii M, Rizi RR, “Improved technique for measurement of regional fractional ventilation by hyperpolarized ^{3}He MRI,” Magnetic Resonance in Medicine, vol. 63, no. 1, pp. 137–150, 2009.

[20]. Deninger AJ, Månsson S, Petersson JS, Pettersson G, Magnusson P, Svensson J, Fridlund B, Hansson G, Erjefeldt I, Wollmer P, et al., “Quantitative measurement of regional lung ventilation using ^{3}He MRI” Magnetic Resonance in Medicine, vol. 48, no. 2, pp. 223–232, 8 2002. [PubMed: 12210930]

[21]. Imai H, Matsumoto H, Miyakoshi E, Okumura S, Fujiwara H, Kimura A, “Regional fractional ventilation mapping in spontaneously breathing mice using hyperpolarized ^{129}Xe MRI,” NMR in Biomedicine, pp. 24–29, 10 2014. [PubMed: 25312654]

[22]. Haczku A, Emami K, Fischer MC, Kadlecek S, Ishii M, Panettieri RA, Rizi RR, “Hyperpolarized 3He MRI in asthma,” Academic Radiology, vol. 12, no. 11, pp. 1362–1370, 11 2005 [PubMed: 16253848]

[23]. Jameson CJ, Jameson AK, Hwang JK, "Nuclear spin relaxation by intermolecular magnetic dipole coupling in the gas phase. ^{129}Xe in oxygen," The Journal of Chemical Physics, vol. 89, no. 7, pp. 4074–4081, 10 1988

[24]. Gudbjartsson H, Patz S, "The rician distribution of noisy MRI data," Magnetic Resonance in Medicine, vol. 34, no. 6, pp. 910–914, 12 1995. [PubMed: 8598820]

[25]. Ruppert K, Brookeman JR, Hagspiel KD, Mugler JP, "Probing lung physiology with xenon polarization transfer contrast (XTC)," Magnetic Resonance in Medicine, vol. 44, no. 3, pp. 349–357, 9 2000. [PubMed: 10975884]

[26]. Swanson SD, Rosen MS, Coulter KP, Welsh RC, Chupp TE, "Distribution and dynamics of laser-polarized 129Xe magnetization in vivo," Magnetic Resonance in Medicine, vol. 42, no. 6, pp. 1137–1145, 12 1999 [PubMed: 10571936]

[27]. Wolber J, Cherubini A, Leach MO, Bifone A, "Hyperpolarized 129Xe NMR as a probe for blood oxygenation," Magnetic Resonance in Medicine, vol. 43, no. 4, pp. 491–496, 4 2000. [PubMed: 10748422]

[28]. Ruppert K, Amzajerdian F, Hamedani H, Xin Y, Loza L, Achekzai T, Duncan IF, Profka H, Siddiqui S, Pourfathi M, et al., "Assessment of flip angle-TR equivalence for standardized dissolved-phase imaging of the lung with hyperpolarized 129Xe MRI," Magnetic Resonance in Medicine, 10 2018.

[29]. Gómez Damián PA, Sperl JI, Janich MA, Khegai O, Wiesinger F, Glaser SJ, Haase A, Schwaiger M, Schulte RF, Menzel MI, "Multisite kinetic modeling of ^{13}C metabolic MR using [1-^{13}C]Pyruvate," Radiology Research and Practice, vol. 2014, pp. 1–10, 12 2014.

[30]. Sakai K, Bilek AM, Oteiza E, Walsworth RL, Balamore D, Jolesz FA, Albert MS, "Temporal dynamics of hyperpolarized 129Xe resonances in living rats," Journal of Magnetic Resonance, Series B, vol. 111, no. 3, pp. 300–304, 6 1996. [PubMed: 8661297]

[31]. Freeman MS, Cleveland ZI, Qi Y, Driehuys B, "Enabling hyperpolarized ^{129}Xe MR spectroscopy and imaging of pulmonary gas transfer to the red blood cells in transgenic mice expressing human hemoglobin" Magnetic Resonance in Medicine, vol. 70, no. 5, pp. 1192–1199, 11 2013. [PubMed: 24006177]

[32]. Reza AM, "Realization of the contrast limited adaptive histogram equalization (CLAHE) for real-time image enhancement," The Journal of VLSI Signal Processing-Systems for Signal, Image, and Video Technology, vol. 38, no. 1, pp. 35–44, 8 2004.

[33]. Wakayama T, Kitamoto M, Ueyama T, Imai H, Narazaki M, Kimura A, Fujiwara H, "Hyperpolarized 129Xe MRI of the mouse lung at a low xenon concentration using a continuous flow-type hyperpolarizing system," Journal of Magnetic Resonance Imaging, vol. 27, no. 4, pp. 777–784, 4 2008. [PubMed: 18383257]

[34]. Wakayama T, Narazaki M, Kimura A, Fujiwara H,, "Hyperpolarized 129Xe phase-selective imaging of mouse lung at 9.4T using a continuous-flow hyperpolarizing system," Magnetic Resonance in Medical Sciences, vol. 7, no. 2, p. 8, 2008.

[35]. Narazaki M, Wakayama T, Imai H, Kimura A, Fujiwara H, "Analysis of hyperpolarized 129Xe dynamics in mouse lungs under spontaneous respiration for separate determination of lung functional parameters and relaxation time," Magnetic Resonance in Medical Sciences, vol. 5, no. 3, pp. 119–128, 2006. [PubMed: 17139137]

[36]. Narazaki M, Wakayama T, Kimura A, Fujiwara H, "MRS of hyperpolarized 129BXe in the chest of mouse-effect of contrast agents on the MRS," International Congress Series, vol. 1265, pp. 177–180, 8 2004.

[37]. Hori Y, Kimura A, Wakayama T, Kitamoto M, Imai F, Imai H, Fujiwara H, "3D hyperpolarized 129Xe MRI of mouse lung at low xenon concentration using a continuous flow-type hyperpolarizing system: Feasibility for quantitative measurement of regional ventilation" Magnetic Resonance in Medical Sciences, vol. 8, no. 2, pp. 73–79, 2009. [PubMed: 19571499]

[38]. Imai H, Kimura A, Hori Y, Iguchi S, Kitao T, Okubo E, Ito T, Matsuzaki T, Fujiwara H, "Hyperpolarized ^{129}Xe lung MRI in spontaneously breathing mice with respiratory gated fast imaging and its application to pulmonary functional imaging," NMR in Biomedicine, vol. 24, no. 10, pp. 1343–1352, 12 2011. [PubMed: 21538635]

[39]. Tetsumoto S, Takeda Y, Imai H, Kimura A, Jin Y, Nakanishi K, Maeda Y, Kuhara H, Tsujino K, Iwasaki T, et al., "Validation of noninvasive morphological and diffusion imaging in mouse emphysema by micro-computed tomography and hyperpolarized ^{129}Xe Magnetic Resonance Imaging," American Journal of Respiratory Cell and Molecular Biology, vol. 49, no. 4, pp. 592–600, 10 2013. [PubMed: 23668642]

[40]. Ford NL, McCaig L, Jeklin A, Lewis JF, Veldhuizen RAW, Holdsworth DW, Drangova M, "A respiratory-gated micro-CT comparison of respiratory patterns in free-breathing and mechanically ventilated rats," Physiological Reports, vol. 5, no. 2, p. e13074, 1 2017. [PubMed: 28100723]

[41]. Santyr GE, Lam WW, Ouriadov A, "Rapid and efficient mapping of regional ventilation in the rat lung using hyperpolarized 3He with flip angle variation for offset of RF and relaxation (FAVOR)," Magnetic Resonance in Medicine, vol. 59, no. 6, pp. 1304–1310, 6 2008. [PubMed: 18506796]

[42]. Couch MJ, Ouriadov A, Santyr GE, "Regional ventilation mapping of the rat lung using hyperpolarized ^{129}Xe magnetic resonance imaging" Magnetic Resonance in Medicine, vol. 68, no. 5, pp. 1623–1631, 11 2012. [PubMed: 22231781]

[43]. Krinke G, The Laboratory Rat. Academic Press, 2000, pp. 323–344.

[44]. Stephen MJ, Emami K, Woodburn JM, Chia E, Kadlecek S, Zhu J, Pickup S, Ishii M, Rizi RR, Rossman M, "Quantitative assessment of lung ventilation and microstructure in an animal model of idiopathic pulmonary fibrosis using hyperpolarized gas MRI," Academic Radiology, vol. 17, no. 11, pp. 1433–1443, 11 2010. [PubMed: 20934126]

[45]. Norquay G, Leung G, Stewart NJ, Wolber J, Wild JM, "^{129}Xe chemical shift in human blood and pulmonary blood oxygenation measurement in humans using hyperpolarized ^{129}Xe NMR" Magnetic Resonance in Medicine, vol. 77, no. 4, pp. 1399–1408, 4 2017. [PubMed: 27062652]

[46]. Zhou X, Mazzanti ML, Chen JJ, Tzeng Y-S, Mansour JK, Gereige JD, Venkatesh AK, Sun Y, Mulkern RV, Albert MS, "Reinvestigating hyperpolarized 129Xe longitudinal relaxation time in the rat brain with noise considerations," NMR in Biomedicine, vol. 21, no. 3, pp. 217–225, 4 2008. [PubMed: 17557274]

[47]. Choquet P, Hyacinthe J-N, Duhamel G, Leviel J-L, Constantinesco A, Ziegler A, "Method to determine in vivo the relaxation time T1 of hyperpolarized xenon in rat brain," Magnetic Resonance in Medicine, vol. 49, no. 6, pp. 1014–1018, 6 2003. [PubMed: 12768578]

[48]. Oregioni A, Parizel N, de Sousa PL, Grucker D, "Fast measurement of relaxation times by steady-state free precession of 129Xe in carrier agents for hyperpolarized noble gases," Magnetic Resonance in Medicine, vol. 49, no. 6, pp. 1028–1032, 6 2003. [PubMed: 12768580]

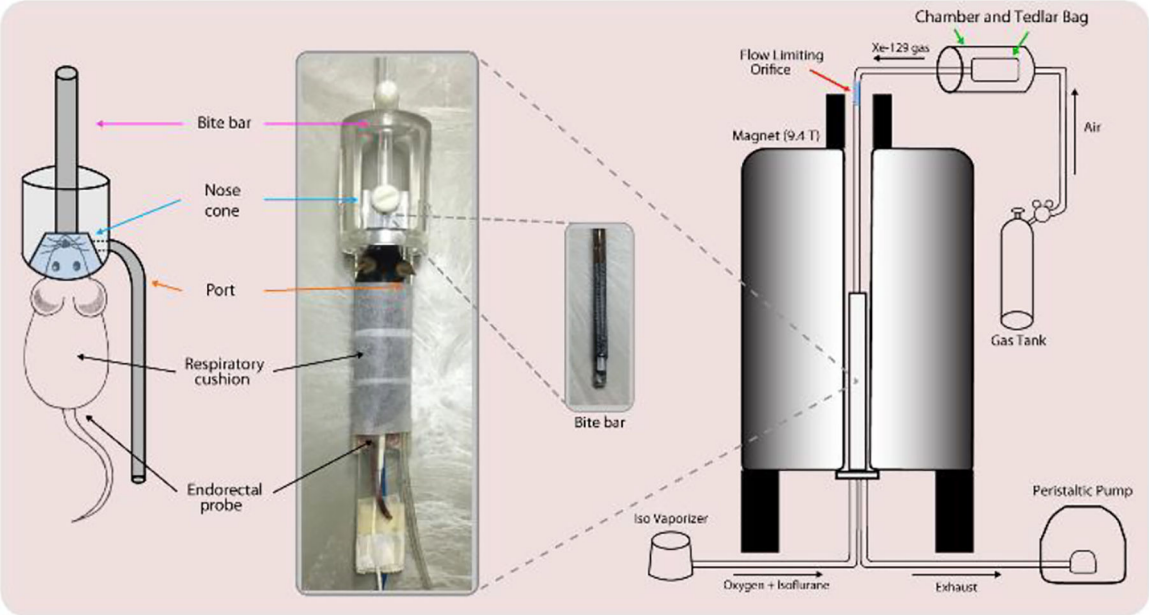

Fig. 1.

(Left) Mice were held in an animal cradle consisting of a bite bar to adjust the animal's position, and a nose cone through which gas is supplied. The port was used as an exhaust for exhaled gas. (Right) O_2, air, and isoflurane were supplied from beneath the bore, while ^{129}Xe was supplied from above through the bite bar: the gases mix within the nose cone, supplying the animal with a normoxic gas mixture. Exhaled gas and isoflurane were passed through a peristaltic pump and isoflurane scrubber.

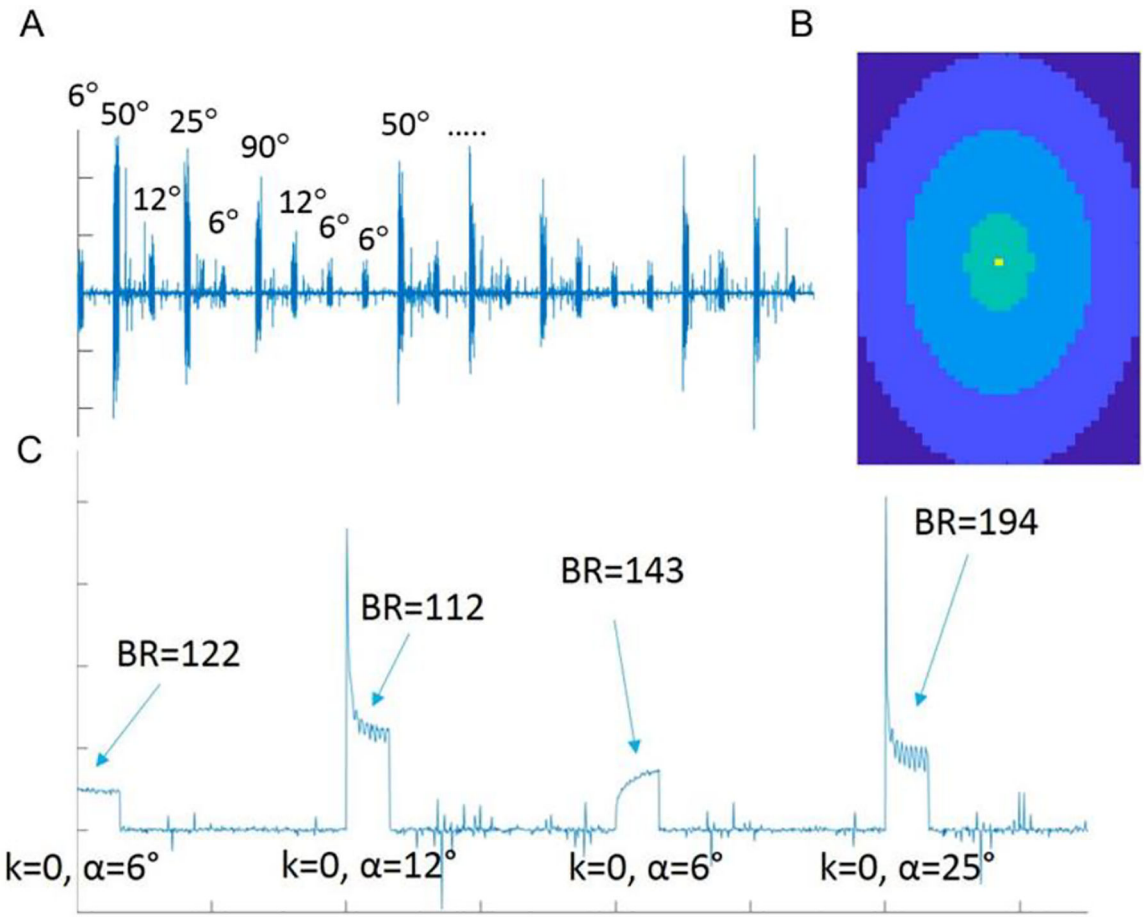

Fig. 2. A)
Sample of raw CSI data. The FA cycles through a set of discrete values over the course of the scan, as reflected by the varying peak signal intensities. **B)** Color map image indicating the relative sampling of k-space points during imaging. Points at or near k = 0 were oversampled the most (six times in yellow, three times in green regions), whereas points further from the center were sampled less (twice and once in the light blue and blue regions, respectively). K-space points corresponding to dark blue regions were not sampled. **C)** Zoomed-in sample of raw CSI data. After switching to a given FA, dummy scans at k = 0 were applied until steady breathing was achieved. Breathing rate and external T_1 decay throughout the entirety of the scan can be extrapolated from data acquired during these dummy scans.

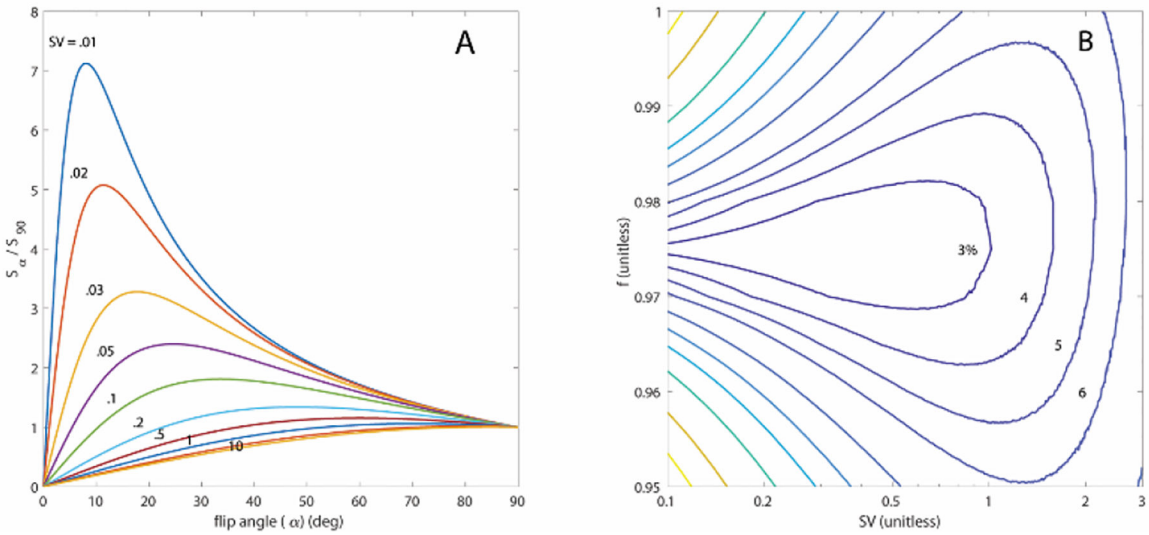

Fig. 3. A)

Plot of image signal dependence on flip-angle (3) for discrete SV values (colored lines). Note that SV may be determined by the ratio of the signal observed at $\alpha = 90°$ to that of any other flip-angle, although the best choice for that flip-angle depends on the expected range of SV. **B)** Contour plots depicting the expected rms % error for individual voxels calculated using (4), and an assumed image S/N of 100 and $\alpha_{ref} = 30°$. This choice distinguishes well among the SV typical of our observations (~0.3 – 0.5) and is acceptable (< 10% error) across the wide range of 0.1–3. This error can increase for inaccurate assumptions about additional relaxation mechanisms represented by *f*, but remains acceptable at typical SV values across the entire physiologically plausible range of 0.95 – 1.

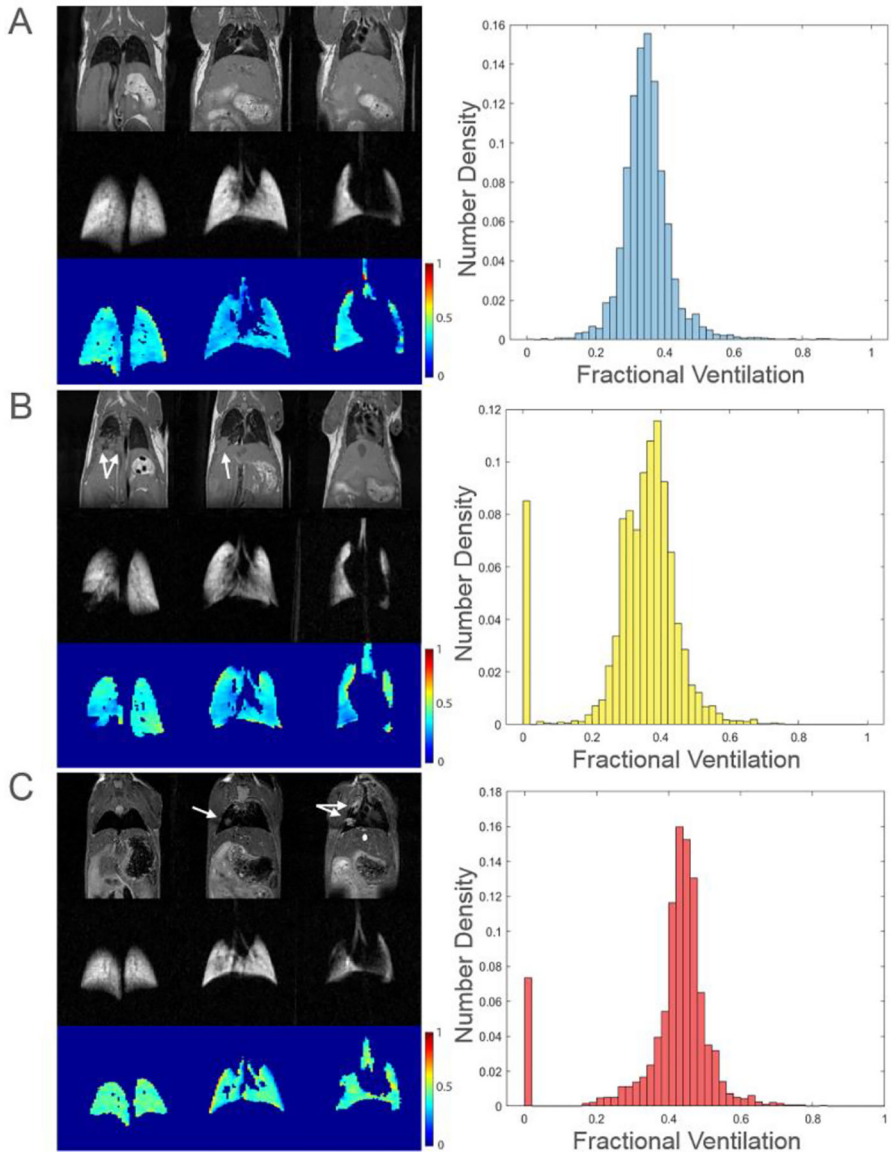

Fig. 4.

T_2-weighted proton images, high-resolution GP images, and FV maps with corresponding histograms for three representative mice are shown above. Regions corresponding to tumors are indicated by white arrows. FV values of 0 (seen in histograms B and C) are derived from cancerous regions where there is no ventilation.

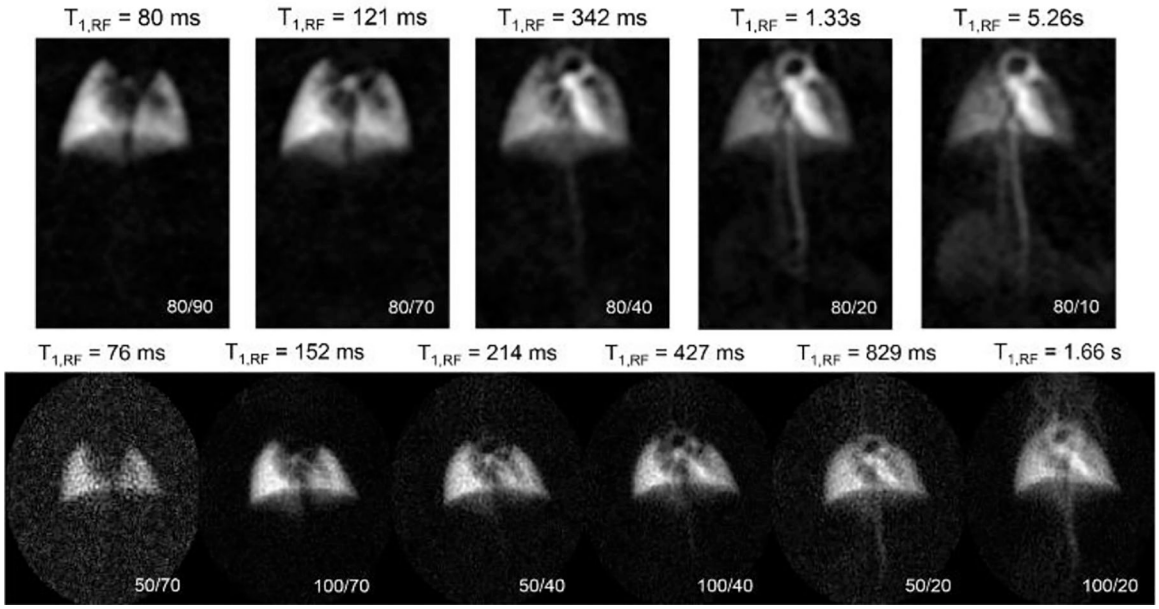

Fig. 5.

DP images acquired using CSI (top) and UTE (bottom) sequences with effective $T_{1,RF}$ values noted above each image. Various TR/FA combinations (lower right corners) were used to visualize different regions along the cardiopulmonary system: e.g., the CSI image at a TR/FA of 80/10 imparts the least relaxation on ^{129}Xe spins, revealing distal features such as the kidneys that are otherwise invisible in the UTE images.

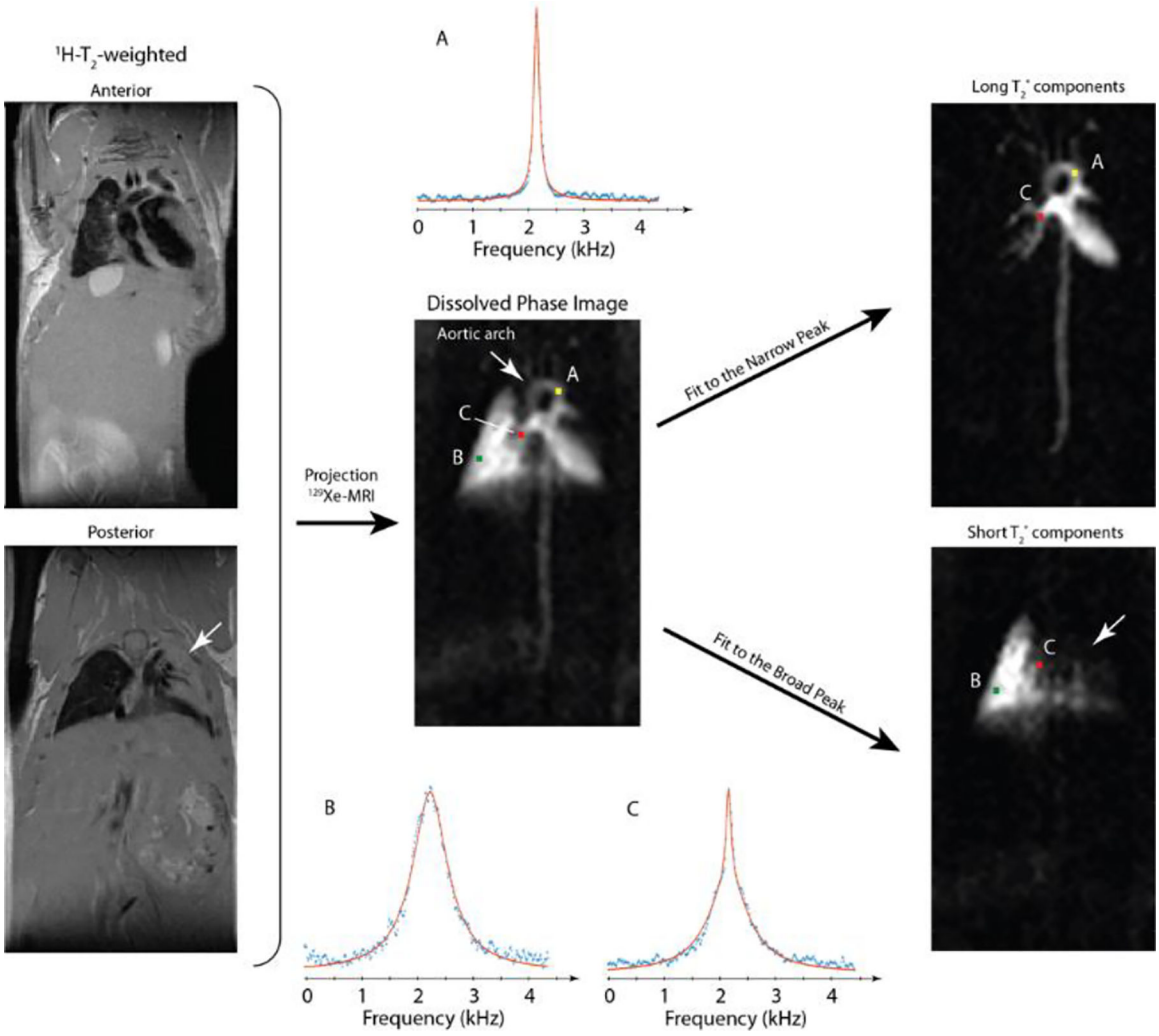

Fig. 6.

Line-shape fitting allows clear discrimination between lung parenchyma and vasculature based on local T_2*. Simple integration of the DP peak (C, center image) masks parenchymal regions in which gas transport is not occurring (white arrows), but narrow (top right) and broad (bottom right) components can be used to highlight the two tissue types separately to remove this ambiguity. Exemplary fits (A, top right image; B, bottom right image) show this procedure in a C57BL/6^{WT} mouse with lung injury (white arrows).

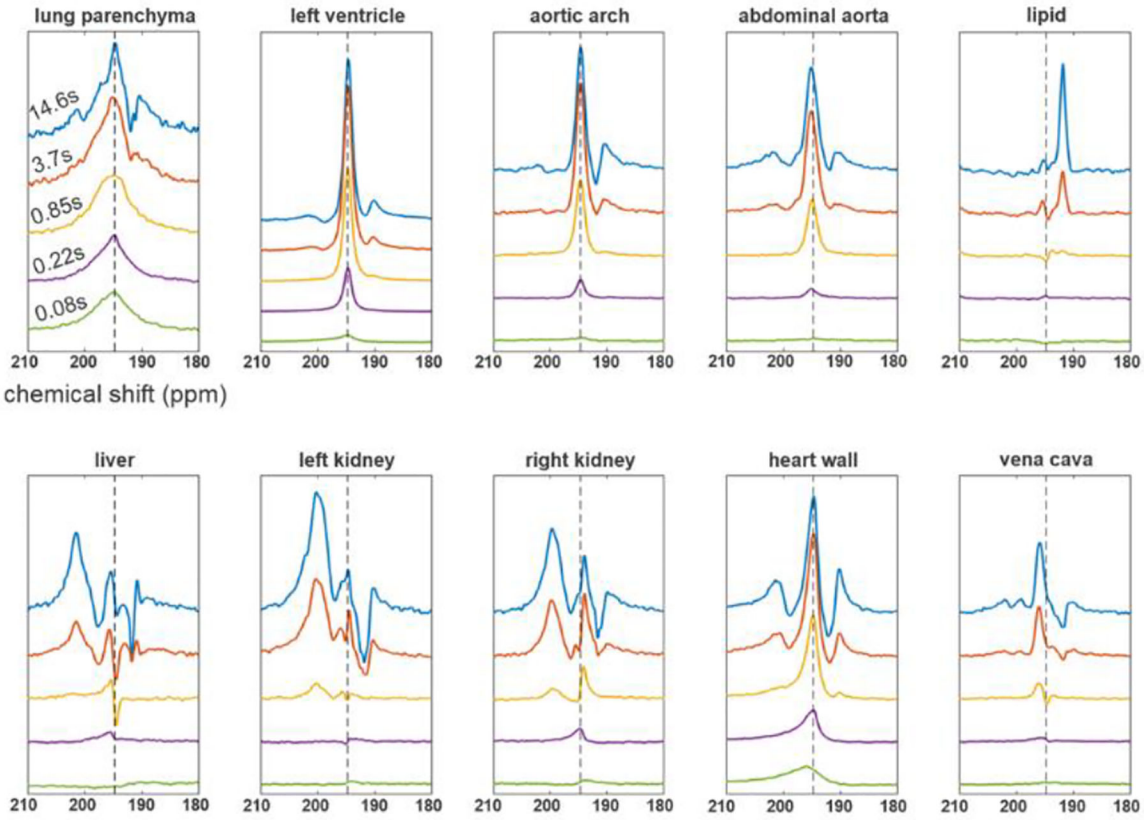

Fig. 7.

DP spectra for various $T_{1,RF}$ values (0.08 s, 0.22 s, 0.85 s, 3.7 s and 14.6 s, bottom to top) for respectively colored regions of interest. DP ^{129}Xe spectra in the lung parenchyma for short $T_{1,RF}$ values predominantly show wide spectral contributions centered at 194.5 ppm (dashed line); however, as we move to longer $T_{1,RF}$ values, spectral contributions from adjacent anatomical structures become visible. Spectra from regions further away from the lungs, such as kidneys and fat, exhibit both longer appearance times as well as separate, tissue-specific spectral contributions.

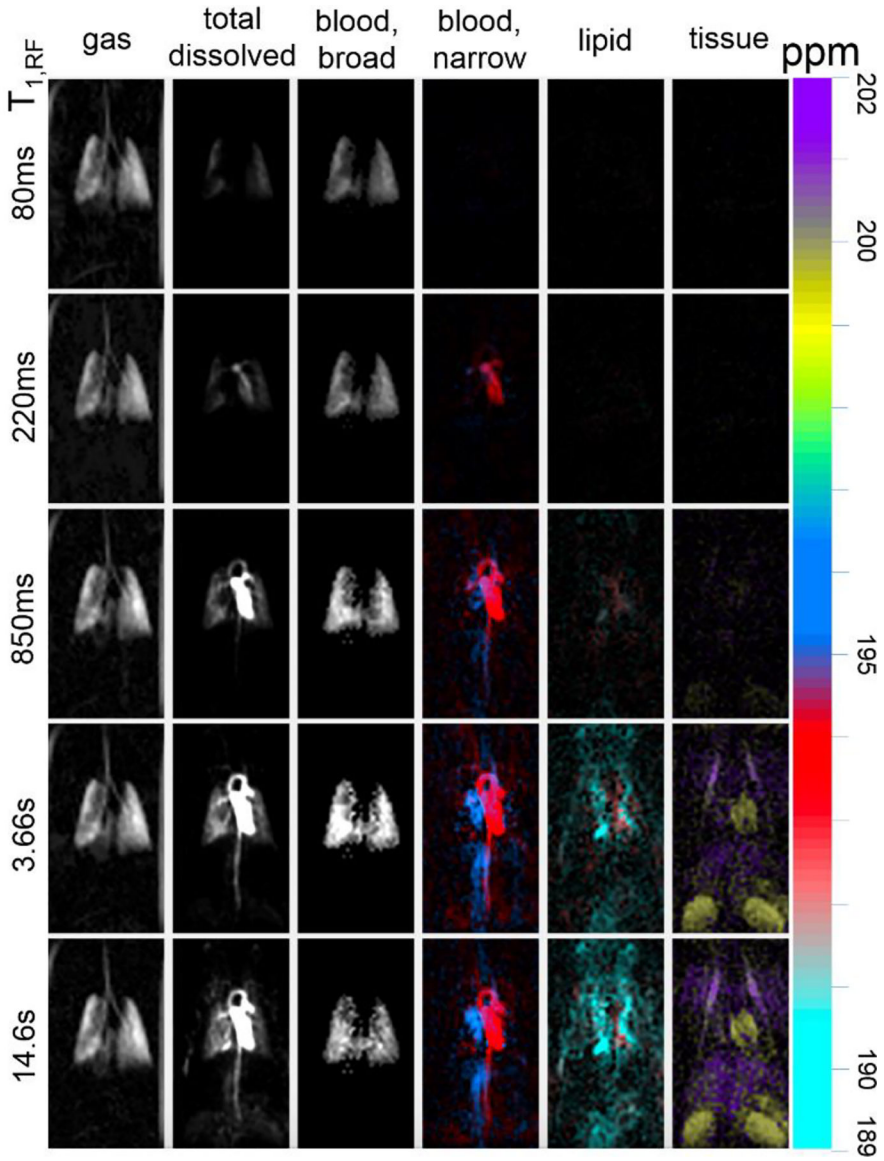

Fig. 8.

Distinct “compartmental” features along the circulatory system can be visualized by integrating under respective DP linewidth peaks. $T_{1,RF}$ times (left) correspond to how long ^{129}Xe magnetization persists in the body and, consequently, how far within the body it travels. The large range in chemical shifts associated with DP ^{129}Xe entering distinct anatomical compartments is visualized in individual, color-coded maps.

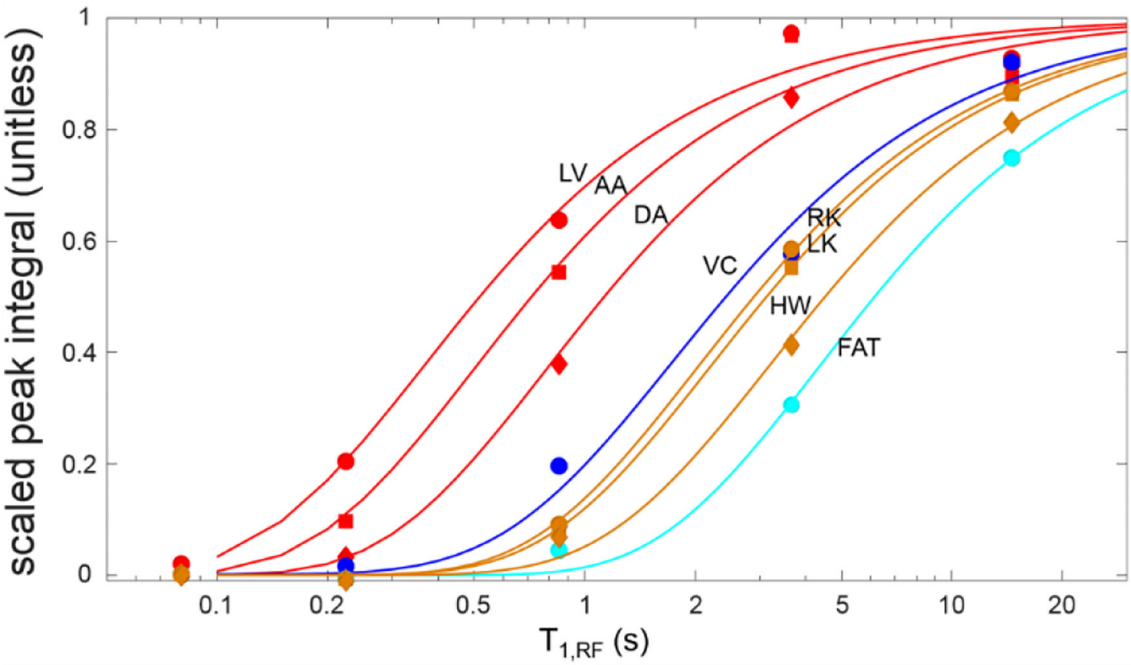

Fig. 9.

Quantification of magnetization buildup in the left ventricle (red circles, $\bar{T}$ = 360 ms), aortic arch (red squares, $\bar{T}$ = 490 ms), descending aorta (red diamonds, $\bar{T}$ = 790 ms), vena cava (blue circles, $\bar{T}$ = 1.7 s), left and right kidneys (ochre squares and circles, $\bar{T}$ = 2.2 s and 2.0 s, respectively), heart wall (ochre diamonds, $\bar{T}$ = 3.2 s) and lipid-rich regions (cyan circles, $\bar{T}$ = 4.8 s). The lines indicate fits to the two-parameter model of gas dissolution duration of (5) and (6). All spectral peak integrals are scaled to the saturation value indicated by the fit. Note that the dissolved gas can be seen in the heart even with a very short $T_{1,RF}$, indicating a rapid arrival in accordance with accepted physiological understanding. Arrival in more distal vascular structures indicates the rate at which blood is transported after leaving the heart, and arrival/saturation of organ tissues mirrors the relatively slow saturation by oxygen or other dissolved gases.